Int. J. Electrochem. Sci., 15 **(2020)** 9487 – 9498, doi: 10.20964/2020.08.100

International Journal of
ELECTROCHEMICAL
SCIENCE
www.electrochemsci.org

An Enhanced Li_3AlH_6 Anode Prepared by a Solid-State Ion Exchange Method for Use in a Solid-State Lithium-Ion Battery

Sangpu Yang, Haozheng Wang, Han Man, Ziyao Long, Jinghao Yang, Shuxian Sun, Jiafeng Ruan, Yun Song and Fang Fang[*]

Department of Materials Science, Fudan University, Shanghai, 200433, China
[*]E-mail: f_fang@fudan.edu.cn

Received: 2 May 2020 / Accepted: 27 June 2020 / Published: 10 August 2020

Li_3AlH_6 is an anode material with an enormous potential to enhance the energy density of secondary lithium-ion batteries that is limited by severe irreversibility and instability. In this study, a high-performance Li_3AlH_6 anode is synthesized via a solid-state ion exchange reaction between a $LiBH_4$ electrolyte and Na_3AlH_6. This reaction not only forms a tight contact between Li_3AlH_6 and $LiBH_4$ but also introduces a $NaBH_4/LiBH_4$ electrolyte layer with excellent Li^+ conductivity around Li_3AlH_6. The as-synthesized Li_3AlH_6 anode exhibits a first discharge capacity of 1722 $mAh\cdot g^{-1}$ and a capacity loss of only 15% in the first charge. After 150 cycles under a current density of 1 $A\cdot g^{-1}$, the Li_3AlH_6 anode retains a capacity of 990 $mAh\cdot g^{-1}$ with nearly 100% coulombic efficiency. An anomalous increase in the capacity during cycling is analyzed and attributed to effects from Al electrochemical milling on the active material.

Keywords: Lithium-ion batteries; Hydride anode; Li3AlH6; Electrochemical properties; All-solid-state batteries

1. INTRODUCTION

Lithium ion batteries (LIB) are being increasingly used as power sources in electric or hybrid vehicles, and demand for a high energy density has continued to grow [1, 2]. To meet this demand, metal hydrides have emerged as a novel anode material for LIBs. Oumellal[3] have reported a general conversion reaction of MgH_2 with lithium:

$$M_a(M'_b)H_x + xLi^+ + xe^- \Leftrightarrow aM\ (+\ bM') + xLiH \qquad (1)$$

This reaction also occurs for other metal hydrides, including TiH_2 and AlH_3, and complex hydrides, such as Mg_2FeH_6, and $NaAlH_4$ [4-7]. Among these hydrides, alanates deserve special consideration relatively higher reversibilities and high hydrogen proportions, which indicate a high reversible lithium ion capacity, i.e., 2119 mAh/g for $LiAlH_4$ and 1985 mAh/g for $NaAlH_4$ [5, 7].

Unfortunately, the reported cycling reversibility of alanates appears to be very poor, where only 20% of the discharge capacity is recovered in the first charge [5, 8, 9]. In previous research studies, two reasons have been identified to explain this result. First, the lithiation of alanates is a multistep process, of which the first step (the conversion of Li_3AlH_6 to $LiAlH_4$) has been shown to be irreversible by both DFT calculations and potentiostatic cycling results [5]. Second, and more importantly, the H ion in alanate has a negative valence and is thus highly reducible and easily oxidized by an organic liquid electrolyte. Therefore, it is vital to provide a reductive chemical environment for alanate to improve cycling stability. In previous reports, $LiAlH_4$, $LiNa_2AlH_6$, MgH_2 and Mg_2FeH_6 anodes have been shown to function effectively with a reductive $LiBH_4$ solid electrolyte [5, 6, 10-12]. The high Li^+ conductivity, wide working potential and stable reductive environment of the $LiBH_4$ electrolyte [13-16] clearly improved the cycling stability of alanates. For instance, the specific capacity of $LiNa_2AlH_6$ loaded on 3D graphite with a $LiBH_4$ electrolyte is 900 $mAh\cdot g^{-1}$ after 500 charge/discharge cycles for a current rate of 1 $A\cdot g^{-1}$ [10].

Although the introduction of a reductive solid borohydride electrolyte has considerably improved the lithium storage performance of alanates, the high solid-solid interfacial resistance between active materials and electrolytes presents a significant disadvantage [17-19]. In contrast to the good infiltration of liquid electrolytes, poor physical contact with heterogeneous contact points at the interface of active materials and solid electrolytes, as well as the volume expansion and shrinkage of active materials upon electrochemical cycling, results in physical degradation, such as contact loss or crack formation [17-21]. Numerous studies have been performed to develop various methods for improving solid-solid interfacial contact. One effective approach is to create a solid-liquid interface, followed by the formation of a solid-solid interface via solidification, deposition or in situ growth. For example, in a study by Zhang, a gel polymer electrolyte is solidified using a commercial $LiFePO_4$ cathode and in situ ultraviolet irradiation to produce an intimate interface with low resistance [22]. However, this method is inapplicable to $LiBH_4$ and alanates, which have close decomposition and melting temperatures and poor solubilities in organic solvents. Another effective technique is to create an interfacial transition layer by the direct reaction of two solid materials, i.e. an active material and an electrolyte. For instance, Unemoto[23] have reported a $TiS_2/LiBH_4/Li$ all-solid-state battery, wherein ban in situ reaction between TiS_2 and a $LiBH_4$ electrolyte forms a robust $Li_2B_{12}H_{12}$ interlayer that stabilizes the surface connection and protects the solid electrolyte from decomposition. However, the reported Li^+ conductivity of $Li_2B_{12}H_{12}$ is two orders of magnitude lower than that of the high-temperature phase of $LiBH_4$, and the resulting deceleration in the transport of lithium ions across the interface deteriorates the rate performance. Therefore, forming an interfacial transition layer with high Li^+ conductivity between the active material and the $LiBH_4$ solid electrolyte remains considerably challenging.

Studies on $LiBH_4$ electrolytes have shown that doping with alkali borohydrides can enhance the Li^+ conductivity. For example, the Li^+ conductivity of a $3LiBH_4$-$NaBH_4$ composite reaches 10^{-2} $S\cdot cm^{-1}$ at 120 °C, which is one order of magnitude higher than that of pure $LiBH_4$ [24]. However, in a study on the hydrogen storage performance of alanates and borohydrides, an ion-exchange reaction between Na_3AlH_6 and $LiBH_4$ induced by ball-milling was observed [25]:

$$Na_3AlH_6 + 3LiBH_4 \rightarrow Li_3AlH_6 + 3NaBH_4 \qquad (2)$$

Motivated by the two considerations above, a lithium battery based on a Li_3AlH_6 anode/$LiBH_4$ electrolyte is prepared in this study, and the lithium storage performance of Li_3AlH_6 anode is investigated. Li_3AlH_6 is prepared by the ion-exchange of Na_3AlH_6 and $LiBH_4$, and the byproduct $NaBH_4$ is dispersed as a dopant into the $LiBH_4$ electrolyte to form an enhanced interfacial transition layer around the prepared Li_3AlH_6 anode. Solid-state ion exchange maintains effective solid-solid interface contact, while enhancing the transport of lithium ions. The prepared Li_3AlH_6 anode reaches a high capacity of 1722 $mAh\cdot g^{-1}$ in the first discharge cycle and retains 990 $mAh\cdot g^{-1}$ after 150 cycles for a current rate of $1A\cdot g^{-1}$. An anomalous increase in the capacity with cycling is found, which is ascribed to Al electrochemical milling.

2. EXPERIMENTAL

2.1 Synthesis of anode composite

LiH, NaH, $NaAlH_4$, $LiAlH_4$ and $LiBH_4$ were purchased from Sigma-Aldrich (purity > 95%) and used as raw materials without further purification. Na_3AlH_6 and Li_3AlH_6 were prepared by ball milling mixtures of 2NaH/$NaAlH_4$ and 2LiH/$LiAlH_4$, respectively. The ball-milling process was performed in a planetary mill (Pulverisette 6, Fritsch) for 20 h at a rotating speed of 500 rpm under an argon atmosphere. The as-synthesized Li_3AlH_6 and Na_3AlH_6 were of high purity. The as-prepared Na_3AlH_6 was thereafter milled with $LiBH_4$ in a 1:9 molar ratio for 5 h at a rotating speed of 500 rpm to fabricate a Li_3AlH_6/$LiBH_4$/$NaBH_4$ composite anode (denoted as LLN). For comparison, a reference sample was prepared as follows: a $LiBH_4$+$NaBH_4$ composite was formed by ball-milling $LiBH_4$ and $NaBH_4$ in a 3:1 molar ratio for 2 h and then further ball-milled with Li_3AlH_6 in a molar ratio of Al:B = 1:9 for 5 h to prepare an ex situ Li_3AlH_6/$LiBH_4$+$NaBH_4$ composite anode (denoted as LL+N). Finally, 25 wt% Super P was added as a conductive agent to both the LLN and LL+N composites. All the operations were carried out in a glove box (Mikrouna SUPER) in an argon atmosphere with H_2O and O_2 concentrations below 1 ppm.

2.2 Materials characterization

The crystal structure of the samples was identified by X-ray diffraction (XRD, Bruker D8 Advance X-ray diffractometer) with Cu Kα radiation (= 1.5406 Å). Scotch tape was used to cover the glass sample cell to prevent sample contamination by air or moisture during measurement. Fourier transform infrared spectroscopy (Nicolet iS50 FT-IR) was also used to investigate the sample structure over 32 scans in a transmission mode. The morphologies and elemental distributions of the samples were investigated using a field emission scanning electron microscope (FEI Quanta FEG 250) with an attached energy dispersive spectrometer (EDS).

2.3 Battery assembly

The electrochemical performance of the LLN and LL+N composite anode materials and the raw Li_3AlH_6 anode material was tested by using a self-designed cell (Φ 12.7 mm), using stainless steel foil as a current collector and PEEK as the shell. A mass of 100 mg of $LiBH_4$ powder was first ground and pressed under 60 MPa to serve as the solid electrolyte: the mixed active materials were then uniformly spread on one side of the pressed $LiBH_4$, and a 0.1-mm-thick Li metal foil was placed on the other side. The obtained cell was pressed under 240 MPa, and this pressure was maintained during the entire electrochemical test.

2.4 Electrochemical measurements

Galvanostatic discharge/charge measurements were conducted using a LANHE CT3001A tester. Electrochemical impedance spectroscopy (EIS) was conducted on a Gamry Interface 1000E. A temperature of 125 °C was used for all the electrochemical measurements to realize high Li^+ conductivity of $LiBH_4$. The current densities and specific capacities were calculated based on the mass of Li_3AlH_6 in the anodes.

3. RESULTS AND DISCUSSION

Figure 1 shows the XRD patterns and FTIR spectra of the LLN and LL+N composites. In Figure 1a for LLN, only Li_3AlH_6, $LiBH_4$ and $NaBH_4$ are detected. The absence of a Na_3AlH_6 phase in the LLN composite demonstrates that all the Na_3AlH_6 has been converted into Li_3AlH_6 and $NaBH_4$ by an ion-exchange reaction with excess $LiBH_4$. For LL+N, the original phase compositions, i.e., Li_3AlH_6, $LiBH_4$ and $NaBH_4$ are observed, and no chemical reaction occurs among these hydrides during ball-milling. The phase compositions of the two composites are further confirmed by the respective FT-IR spectra in Figure 1b. In the IR curves of both LLN and LL+N, B-H stretching and bending peaks appear at 2300 cm^{-1} and 1100 cm^{-1}, respectively, corresponding to the sum of the $LiBH_4$ and $NaBH_4$ peaks [26]. Al-H stretching and bending peaks are detected at approximately 1600-1200 cm^{-1} and 1000-600 cm^{-1}, respectively. The shapes of the XRD and IR curves are perfectly matched, implying identical chemical compositions for LLN and LL+N in the two composites. However, different interfacial characteristics for LLN and LL+N are observed for Li_3AlH_6 and the electrolyte. In LLN, an in situ interface is formed by the ion-exchange reaction of Na_3AlH_6 and $LiBH_4$. The byproduct $NaBH_4$ is doped into excess $LiBH_4$ to form a $NaBH_4/LiBH_4$ composite electrolyte around Li_3AlH_6, where the $NaBH_4$ concentration gradually decreases from the surface of Li_3AlH_6 to the $LiBH_4$ electrolyte, as shown in Figure 2a and b. In contrast with LLN, $NaBH_4$ in LL+N is uniformly dispersed in $LiBH_4$, as shown in Figure 2c, and the interface between Li_3AlH_6 and the electrolyte is still formed by ball-milling the two solid hydrides.

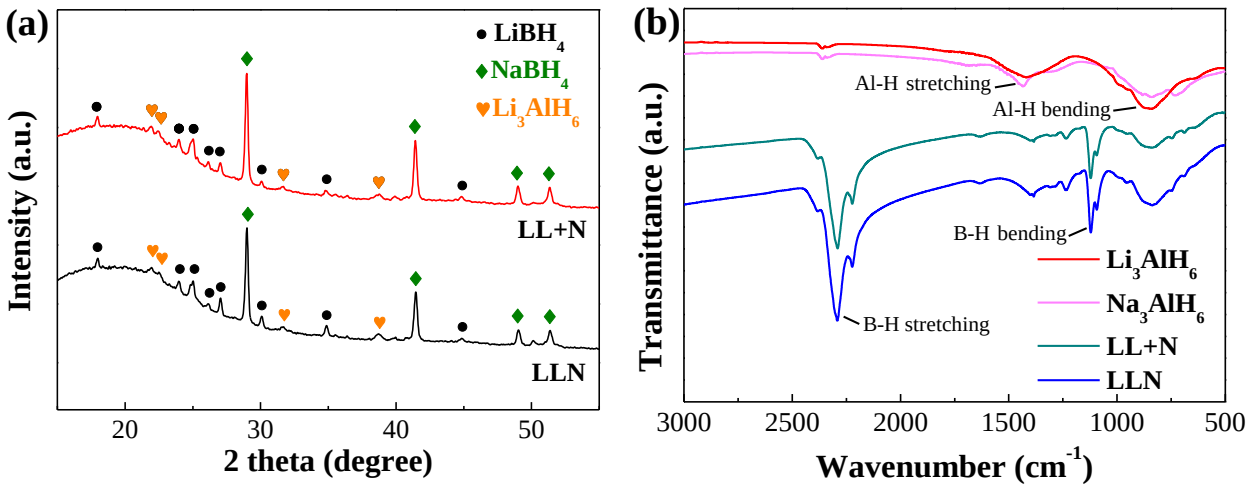

Figure 1. (a) XRD patterns of LLN and LL+N and (b) FT-IR patterns of LLN, LL+N, Li_3AlH_6 and Na_3AlH_6

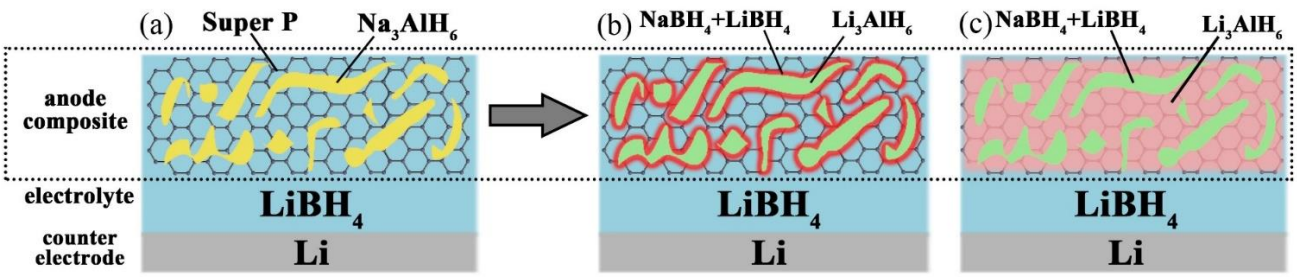

Figure 2. Schematic of chemical composition: (a) original LLN; (b) LLN after ion-exchange reaction; and (c) LL+N in $LiBH_4$ ASS battery

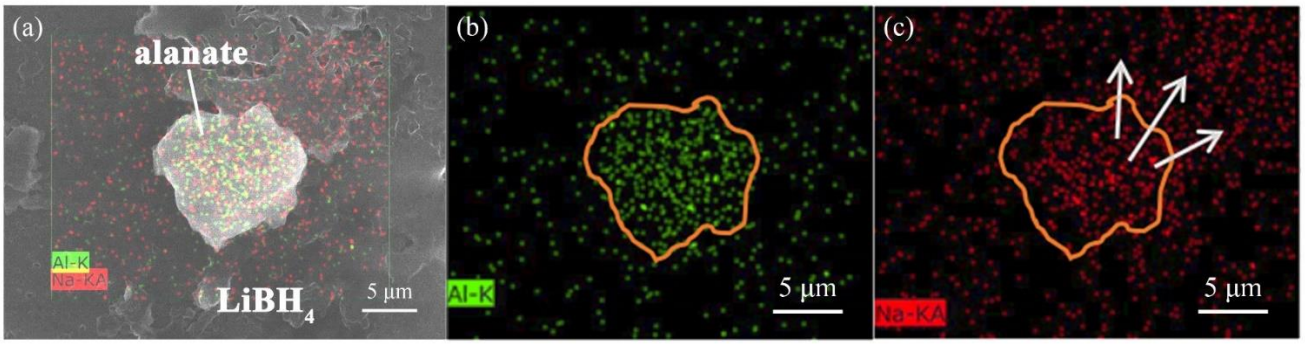

Figure 3. Original Na_3AlH_6 particle on $LiBH_4$ substrate: (a) SEM image and EDS mapping results for elemental (b) Al and (c) Na

Figure 3 shows the results of an additional SEM-EDS experiment that was performed to further explore the ion-exchange reaction of Na_3AlH_6 and $LiBH_4$. Na_3AlH_6 powder was sprinkled on the upper surface of a $LiBH_4$ tablet and subsequently loaded at 240 MPa for 24 h in the glove box to ensure that the Na_3AlH_6 particles were closely embedded in $LiBH_4$. An alanate particle is shown as a representative

example of Na^+ and Li^+ exchange. The EDS results in Figure 3b and c clearly show that elemental Al is mainly locked inside the alanate particle, whereas elemental Na diffuses from the alanate into $LiBH_4$ by an ion exchange process, confirming the in situ formation of the $NaBH_4/LiBH_4$ composite electrolyte around Li_3AlH_6 in LLN.

Table 1. Comparison of the electrochemical performances of representative reported alanates anodes with that of present LLN anode

Anode sample	Synthesis method	Current rate	1st discharge/charge capacity ($mAh \cdot g^{-1}$)	Reversibility (char/dis)	Cycle number	Ref.
$LiAlH_4$	Grinding	C/30	2264/740	32 %	10	[8]
$LiAlH_4$	Grinding	C/20	1180/188	10 %	N/A	[5]
$LiAlH_4$	Ball-milling	C/20	1167/460	39 %	N/A	[5]
$NaAlH_4$	Ball-milling	C/20	1778/1250	70 %	N/A	[8,27]
$NaAlH_4$	Melt infiltration into carbon scaffolds	C/10	2065/1454	70 %	20	[28]
$NaAlH_4$	THF infiltration into carbon scaffolds	20 mA g^{-1} (~C/100)	966/527	54 %	20	[9]
Li_3AlH_6	Ball-milling	C/20	900/198	22 %	N/A	[5]
Na_3AlH_6	Ball-milling	C/20	696/202	29 %	N/A	[8]
$LiNa_2AlH_6$	Ball-milling	C/20	1872/638	34 %	N/A	[8]
$LiNa_2AlH_6$	Solvothermal/ Ball-milling	1 A g^{-1}	3028/1673	55 %	500	[10]
Li_3AlH_6 (LLN)	Ball-milling/ in-situ ion exchange	1 A g^{-1} (~C/2)	1724/1466	85 %	150	This work

To exclude the influence of $NaBH_4$ on the lithium storage capacity, an electrochemical measurement of $NaBH_4/2LiBH_4$ with 25 wt% Super P was carried out: the result in Figure 4 shows that only Super P delivers a low capacity of 94 $mAh \cdot g^{-1}$, and $NaBH_4$ is inactive in lithiation/delithiation. In Figure 5a and b, the galvanostatic discharge-charge (GDC) curves of LLN and LL+N are compared for a current rate of 1 $A \cdot g^{-1}$. The replacement of an organic liquid electrolyte [5-7, 9, 27, 28] with the $LiBH_4$ electrolyte results in high capacity retention and good reversibility over 1-5 cycles for both samples. The capacity retention in the first 2 cycles is 77% for LL+N and increases to 85% for LLN. Similar charging and discharging plateaus can be observed in the GDC curves of LLN and LL+N. The plateaus ca. 0.7 V

in the discharge curve and ca. 0.8 V in the charge curve represent the reversible conversion of Li_3AlH_6 into LiH and Al, and the plateaus ca. 0.25 V in the discharge curve and ca. 0.4 V in the charge curve correspond to the Al-Li alloying process [5].

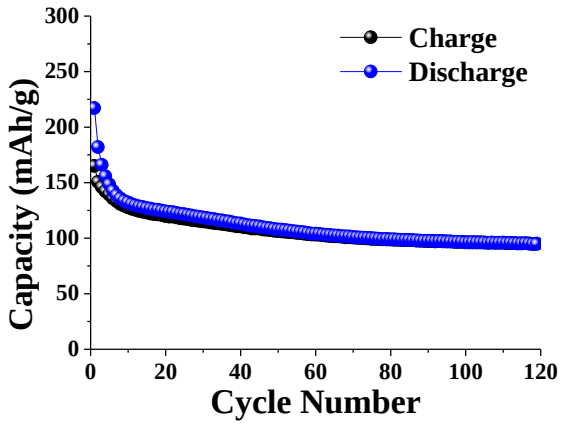

Figure 4. Cycling performance of mixture of $NaBH_4$ and Super P used as anode material

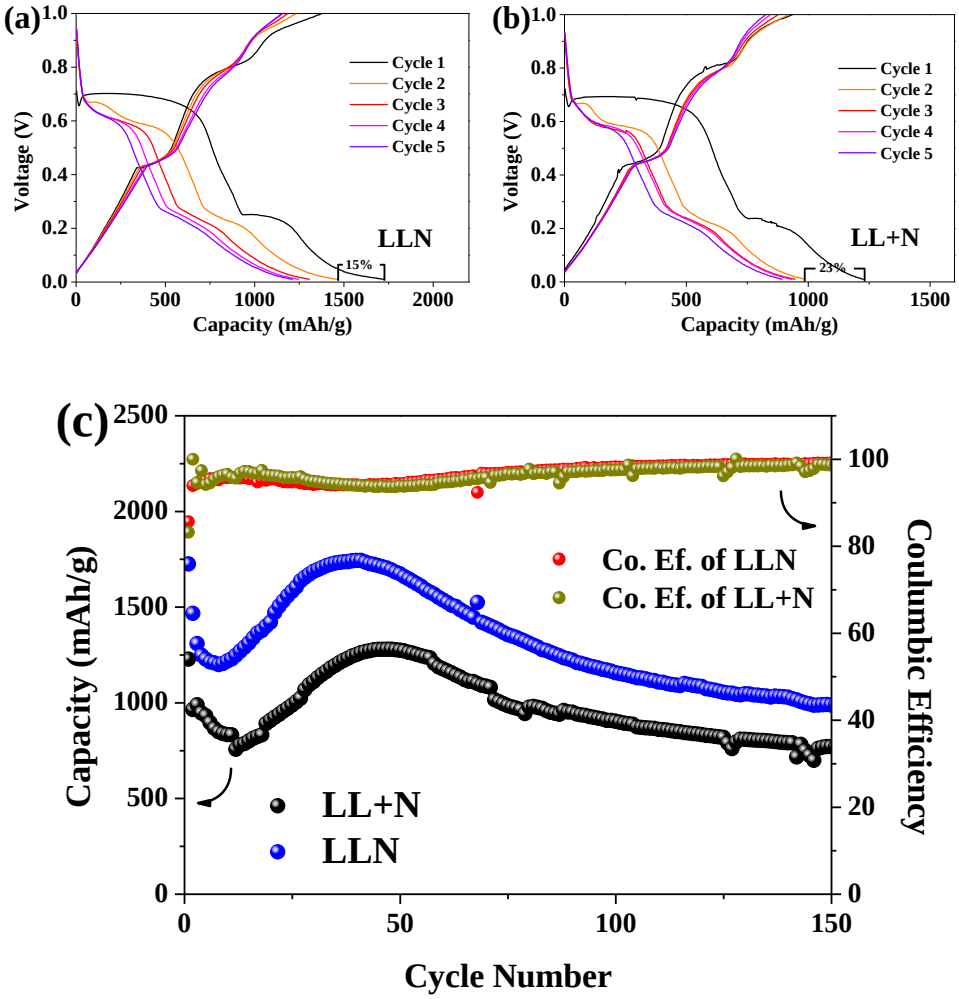

Figure 5. Galvanostatic discharge-charge curves of (a) LLN and (b) LL+N; and (c) cycling performance of LLN, LL+N and LL between 0.01-1.0 V under current rate of 1 $A \cdot g^{-1}$

Figure 5c shows that LLN releases a first-discharge capacity of 1722 mAh·g^{-1} and retains 990 mAh·g^{-1} after 150 cycles, whereas LL+N has a first-discharge capacity of 1227 mAh·g^{-1} and retains 767 mAh·g^{-1} after 150 cycles. The lithium storage performance is improved in LLN in comparison with previous reports on alanates in the following table.

Notably, an undesirable phenomenon is observed in LLN and LL+N. Excluding the initial unstable cycles (~10 cycles), the cycling capacity first increases, passes through a maximum and then decreases as the cycle number increases. A similar variation trend in the cycling capacity has also been reported for a transition-metal-oxide anode with an organic liquid electrolyte, which can be attributed to a change in the chemical valence of transition metals or an irreversible reaction between the oxide and the liquid electrolyte. However, no transition metals with variable valence states are present in LLN and LL+N, and previous research on the hydrogen storage performance of Li_3AlH_6 and $LiBH_4$ has shown that no chemical reaction can occur between these two hydrides [29].

To elucidate the mechanism for the increasing capacity of LLN, the variations in the plateau in the GDC curve at 10, 20 and 40 cycles are compared during the rising period in Figure 6. The increasing cycling capacity clearly derives from the extension of the plateau ca. 0.25 V, indicating that cycling enhances Al lithiation and delithiation. Therefore, a pure Al anode was prepared, and the cycling performance of Al/$LiBH_4$/Li battery was tested: the results are shown in Figure 6b. A fairly similar variation trend in the cycling capacity to that of LLN is observed.

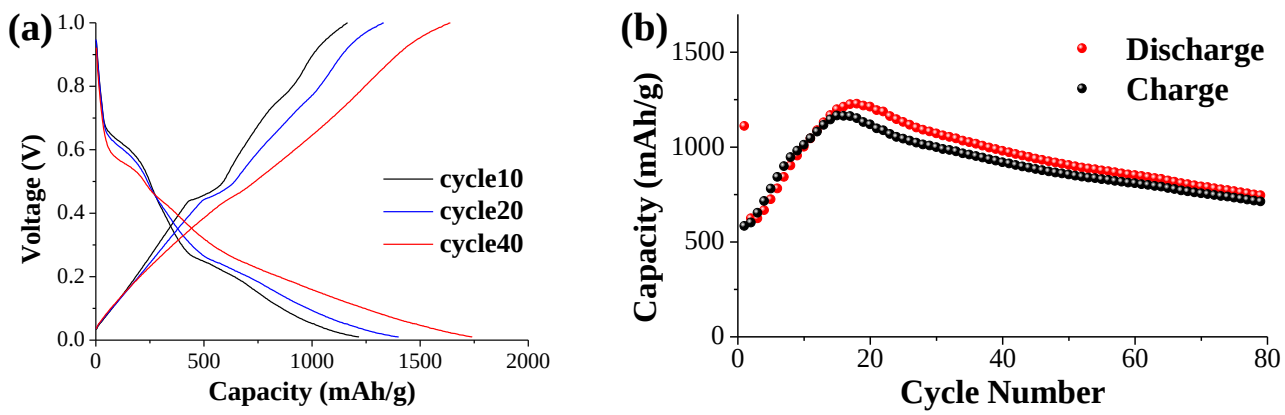

Figure 6. (a) Galvanostatic discharge-charge curve of LLN anode at 10, 20 and 40 cycles and (b) cycling performance of Al between 0.01 and 1 V for current rate of 0.5 A·g^{-1}

The corresponding phase structures of the Al anode in the initial, discharged and recharged states are shown in Figure 7. Apart from the $LiBH_4$ electrolyte, only the Al phase is found in the original anode. When the anode is discharged to 0.01 V, LiAl and Li_3Al_2 phases are observed because of Al lithiation. However, after recharging to 1V, both Al and strong LiAl peaks appear in the XRD pattern, demonstrating that the dealloying process of LiAl is incomplete under the experimental conditions. In a study by Liu and Co [30], similar entrapment was observed in the first discharge/charge cycle of a 16-μm-thick Al foil anode. Neutron depth profiling revealed that a 2-μm-thick α-LiAl layer remained on the Al foil surface after delithiation. The low Li^+ diffusion rate of α-LiAl strongly hindered Li^+ transport

kinetics during the delithiation process, trapping a substantial quantity of Li inside the Al matrix. This may explain the temporary capacity loss in our hand-mixed Al/$LiBH_4$ composite anode during the initial cycles.

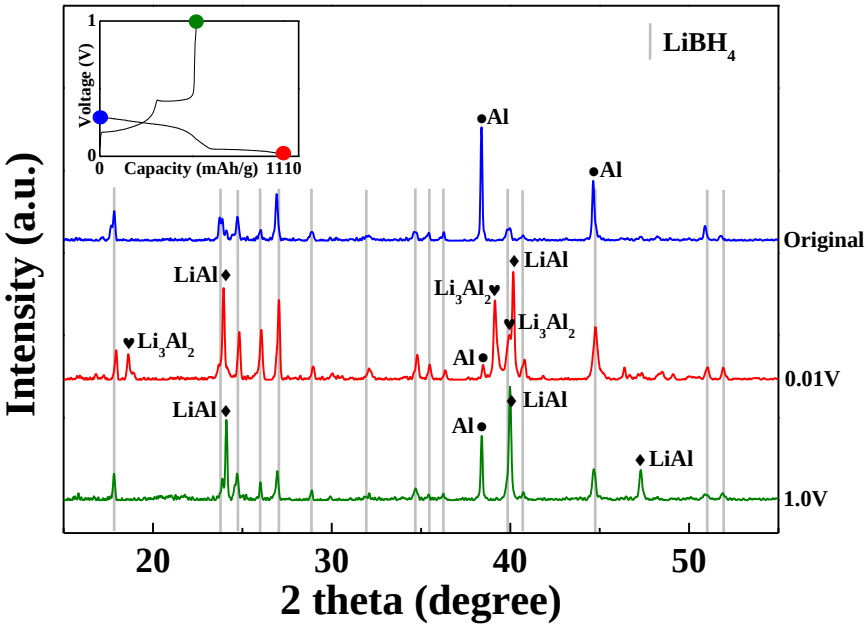

Figure 7. Ex situ XRD test of mechanism of Al anode during first discharge-charge cycle

Recently, Pang[31] proposed a novel solid-solid prelithiation technique for preparing a Li_3AlH_6-Al nanocomposite anode by a short-circuited electrochemical reaction . In this nanocomposite, Al nanograins were uniformly dispersed in an amorphous Li_3AlH_6 matrix, which resulted in a stable cycling capacity. This result implies that reducing the Al particle size could improve the increasing capacity with cycling.

To obtain smaller Al particles, a ball-milling process was used to synthesize the Al/$LiBH_4$ anode, and the cycling performances of the ball-milled and ground Al/$LiBH_4$ anodes were compared. Figure 8 shows that a first discharge capacity of 1267 mAh·g^{-1} is obtained in the ball-milled Al/$LiBH_4$, which is similar to that of the ground Al/$LiBH_4$. As expected, only a 15% capacity loss is observed after the first charge in the ball-milled Al/$LiBH_4$, which is much less than the 48% capacity loss in the ground Al/$LiBH_4$. During the subsequent 15 cycles, the ground Al/$LiBH_4$ capacity gradually increases to almost the same value of the ball-milled Al/$LiBH_4$. Therefore, we speculate that "electrochemical milling" occurs during cycling, as has been reported by Hassan[32]. In the increasing capacity period, the ongoing electrochemical reaction pulverizes the Al particles and exposes more active surfaces, as in the ball-milling process, thus increasing the overall capacity.

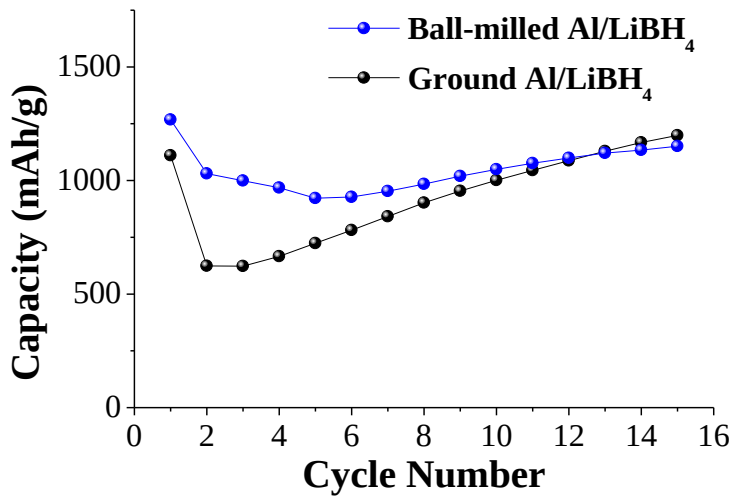

Figure 8. Comparison of cycling performance of ball-milled and hand-ground Al+$LiBH_4$

Electrochemical impedance spectroscopy (EIS) was carried out on both the LLN and LL+N samples to investigate the electrochemical distribution process of Li ions. No semicircles are observed in the high-frequency range of the Nyquist plots of LLN and LL+N in Figure 9a, indicating little resistance in the charge transfer process of the two samples, which is consistent with previous reports for alanate anodes with a $LiBH_4$ electrolyte [10, 31, 33]. The Li^+ diffusion coefficient in the anode composite, was precisely determined by calculating the diffusion coefficients D_{LLN} and D_{LL+N} from the low-frequency range. The following equation can be used to describe the Warburg impedance (Z_w) data in the low-frequency range:

$$Z_w = \frac{k}{\sqrt{\omega}} - j\frac{k}{\sqrt{\omega}} \quad (3),$$

where ω is the frequency, j is $\sqrt{-1}$, and k is the Warburg factor related to the diffusion process. Eq. 3 shows that Z_w depends linearly on $\omega^{-1/2}$: a linear fit of the slope of the low-frequency curves in the Warburg impedance plot produces k-values of 5.21 for LLN and 0.79 for LL+N, as shown in Figure 9b. The Li^+ diffusion coefficient can be determined using the following equation:

$$D_{Li^+} = \frac{R^2T^2}{2n^4F^4C^{B^2}k^2A^2} \quad (4),$$

where R is the ideal gas constant (8.31 $J\cdot mol^{-1}\cdot K^{-1}$), T is the absolute temperature (398 K), n is the number of electrons per molecule (n = 1), F is the Faraday constant (96485 $C\cdot mol^{-1}$), C^B is the Li^+ concentration in the active materials (0.102 $mol\cdot cm^{-3}$), and A is the electrode area (1.267 cm^2). The calculated Li^+ diffusion coefficient in LLN of 3.840×10^{-12} $cm^2\cdot s^{-1}$ is 27 times higher than that of 1.415×10^{-13} $cm^2\cdot s^{-1}$ in LL+N. The superior Li^+ kinetics and the higher cycling performance for the LLN anode prove that solid-state ion exchange enhances the stability of the interface between Li_3AlH_6 and the electrolyte, while increasing lithium ion transport.

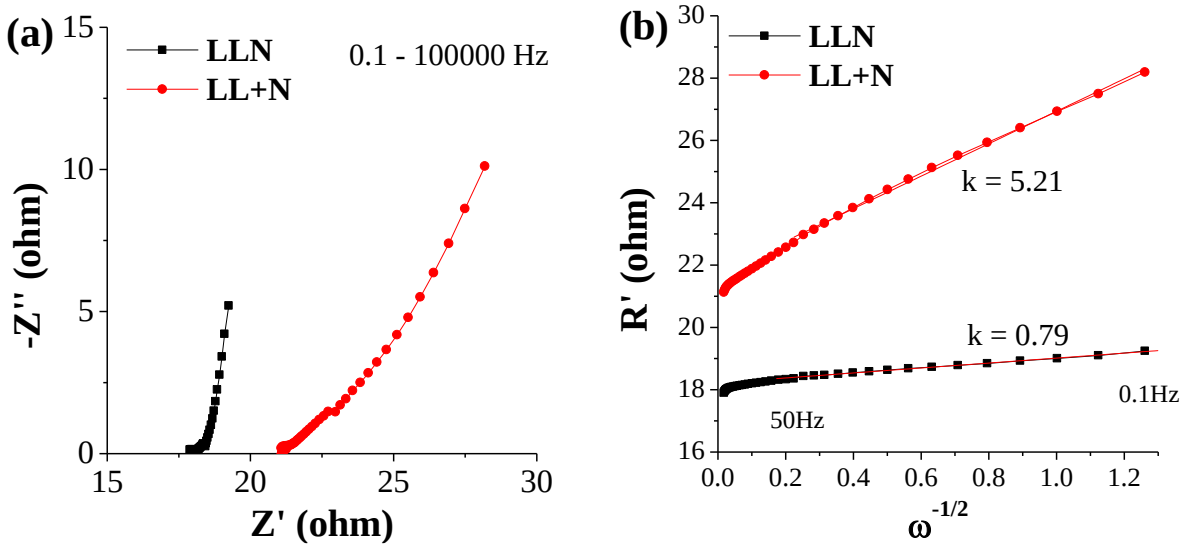

Figure 9. Electrochemical impedance spectra: (a) Nyquist plot and (b) Warburg plot, where linear fit result is measured at open circuit voltage

4. CONCLUSIONS

In summary, we report a facile approach to prepare a structurally enhanced Li_3AlH_6 anode (LLN) with a high capacity and improved reversibility for all-solid-state lithium storage. Li_3AlH_6 is synthesized via an ion-exchange reaction between Na_3AlH_6 and $LiBH_4$ to form a close contact with the solid electrolyte. The byproduct $NaBH_4$ is doped into excess $LiBH_4$ to form a $NaBH_4/LiBH_4$ composite electrolyte around Li_3AlH_6, which shows excellent Li^+ interface conductivity. The LLN anode exhibits an initial discharge capacity of 1722 $mAh\cdot g^{-1}$ at $1A\cdot g^{-1}$ and retains a capacity of 990 $mAh\cdot g^{-1}$ after 150 cycles, which is 30% above that of a mechanically mixed LL+N anode. An increase in the capacity of alanate anodes is observed for the first time: subsequent analysis shows that this phenomenon can be attributed to an electrochemical milling effect during cycling, i.e., the ongoing electrochemical reaction pulverizes Al particles to expose more active surfaces, as in ball-milling, thus increasing the capacity.

ACKNOWLEDGEMENTS
We gratefully acknowledge financial support from the National Natural Science Foundation of China (Grant Nos. 51671058, 51922031 and 51727801).

References

1. Y. Nishi, *Chem. Rec.*, 1 (2001) 406.
2. M. Wakihara, *Mater. Sci. Eng. R: Rep.*, 33 (2001) 109.
3. Y. Oumellal, A. Rougier, G.A. Nazri, J.M. Tarascon and L. Aymard, *Nat. Mater.*, 7 (2008) 916.
4. K. Kawahito, L. Zeng, T. Ichikawa, H. Miyaoka and Y. Kojima, *Mater. Trans.*, 57 (2016) 755.
5. L. Silvestri, S. Forgia, L. Farina, D. Meggiolaro, S. Panero, A. La Barbera, S. Brutti and P. Reale, *ChemElectroChem*, 2 (2015) 877.

6. P. Huen and D.B. Ravnsbæk, *Electrochem. Commun.*, 87 (2018) 81.
7. L. Silvestri, L. Farina, D. Meggiolaro, S. Panero, F. Padella, S. Brutti and P. Reale, *J. Phys. Chem. C*, 119 (2015) 28766.
8. J. A. Teprovich, J. Zhang, H. Colón-Mercado, F. Cuevas, B. Peters, S. Greenway, R. Zidan and M. Latroche, *J. Phys. Chem. C*, 119 (2015) 4666.
9. L. Silvestri, A. Paolone, L. Cirrincione, P. Stallworth, S. Greenbaum, S. Panero, S. Brutti and P. Reale, *J. Electrochem. Soc.*, 164 (2017) A1120.
10. F. Mo, X. Chi, S. Yang, F. Wu, Y. Song, D. Sun, Y. Yao and F. Fang, *Energy Storage Mater.*, 18 (2019) 423.
11. L. Zeng, K. Kawahito, S. Ikeda, T. Ichikawa, H. Miyaoka and Y. Kojima, *Chem. Commun.*, 51 (2015) 9773.
12. L. Zeng, T. Ichikawa, K. Kawahito, H. Miyaoka and Y. Kojima, *ACS Appl. Mater. Interfaces.*, 9 (2017) 2261.
13. M. Matsuo, Y. Nakamori, S.-I. Orimo, H. Maekawa and H. Takamura, *Appl. Phys. Lett.*, 91 (2007) 224103.
14. V. Epp and M. Wilkening, *Phys. Rev. B*, 82 (2010) 020301.
15. M. Matsuo and S.-I. Orimo, *Adv. Energy Mater.*, 1 (2011) 161.
16. R. Mohtadi and S.-I. Orimo, *Nat. Rev. Mater.*, 2 (2016) 16091.
17. H. Yamada, Y. Oga, I. Saruwatari and I. Moriguchi, *J. Electrochem. Soc.*, 159 (2012) A380.
18. K. Yamamoto, Y. Iriyama, T. Asaka, T. Hirayama, H. Fujita, K. Nonaka, K. Miyahara, Y. Sugita and Z. Ogumi, *Electrochem. Commun.*, 20 (2012) 113.
19. J. Haruyama, K. Sodeyama, L. Han, K. Takada and Y. Tateyama, *Chem. Mater.*, 26 (2014) 4248.
20. N. Sun, Q. Liu, Y. Cao, S. Lou, M. Ge, X. Xiao, W.K. Lee, Y. Gao, G. Yin, J. Wang and X. Sun, *Angew. Chem.*, 131 (2019) 18820.
21. S.-K. Jung, H. Gwon, S.-S. Lee, H. Kim, J.C. Lee, J.G. Chung, S.Y. Park, Y. Aihara and D. Im, *J. Mater. Chem. A*, 7 (2019) 22967.
22. S.Z. Zhang, X.H. Xia, D. Xie, R.C. Xu, Y.J. Xu, Y. Xia, J.B. Wu, Z.J. Yao, X.L. Wang and J.P. Tu, *J. Power Sources*, 409 (2019) 31.
23. A. Unemoto, T. Ikeshoji, S. Yasaku, M. Matsuo, V. Stavila, T.J. Udovic and S.-I. Orimo, *Chem. Mater.*, 27 (2015) 5407.
24. M. Xiang, Y. Zhang, L. Zhan, Y. Zhu, X. Guo, J. Chen, Z. Wang and L. Li, *J. Alloys. Compd.*, 729 (2017) 936.
25. F.A.H. Yap, N.S. Mustafa, M.S. Yahya, A.A. Mohamad and M. Ismail, *Int. J. Hydrog. Energy*, 43 (2018) 8365.
26. F.A.H. Yap and M. Ismail, *J. Phys. Chem. C*, 122 (2018) 23959.
27. L. Cirrincione, L. Silvestri, C. Mallia, P.E. Stallworth, S. Greenbaum, S. Brutti, S. Panero and P. Reale, *J. Electrochem. Soc.*, 163 (2016) A2628.
28. P. Huen, F. Peru, G. Charalambopoulou, T.A. Steriotis, T.R. Jensen and D.B. Ravnsbæk, *ACS. Omega*, 2 (2017) 1956.
29. X. Wu, X. Wang, G. Cao, S. Li, H. Ge, L. Chen and M. Yan, *J. Alloys Compd*., 517 (2012) 127.
30. D.X. Liu and A.C. Co, J Am Chem Soc, 138 (2016) 231.
31. Y. Pang, X. Wang, X. Shi, F. Xu, L. Sun, J. Yang and S. Zheng, *Adv. Energy Mater.*, 10 (2020) 1902795.
32. M.F. Hassan, Z. Guo, Z. Chen and H. Liu, *Mater. Res. Bull.*, 46 (2011) 858.
33. H. Liu, Z. Ren, X. Zhang, J. Hu, M. Gao, H. Pan and Y. Liu, *Chem. Mater.*, 32 (2020) 671.